

www.acsanm.org Article

Ab-Initio Studies on Fluorine—Sulfur Coterminated MXene—Reduced Graphene Oxide Composites for Fast Polysulfide Conversion in Flexible Sodium—Sulfur Batteries

Ram Sewak* and Anirban Mondal*



Cite This: https://doi.org/10.1021/acsanm.5c04042



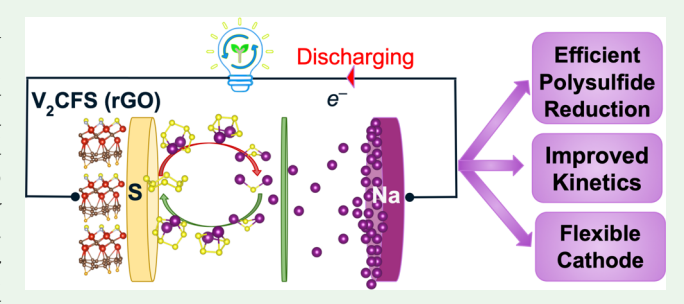
ACCESS I

Metrics & More

Article Recommendations

s Supporting Information

ABSTRACT: Flexible, high-performance cathodes are essential for realizing practical room-temperature sodium—sulfur (Na–S) batteries, yet sluggish polysulfide conversion, poor retention, and mechanical limitations remain major barriers. Here, we introduce a sulfur/fluorine coterminated vanadium carbide MXene integrated with reduced graphene oxide, $V_2CF_{0.67}S_{0.33}$ (rGO), designed to enhance polysulfide anchoring, catalytic activity, and flexibility simultaneously. First-principles calculations reveal that this mixed-termination MXene—rGO composite exhibits markedly stronger polysulfide adsorption (0.8–3.90 eV) than single-terminated counterparts while preserving structural integrity and metallic



conductivity for efficient charge transport. The material achieves the lowest Na₂S decomposition barrier reported for MXene-based Na–S cathodes (0.287 eV) and a reduced Gibbs free energy pathway for the sulfur reduction reaction, enabling faster and more complete sulfur utilization. Charge density difference, partial density-of-states, and crystal orbital Hamilton population analyses confirm substantial charge transfer and strong interfacial chemical bonding with Na₂S_n species. Mechanical stress–strain simulations further demonstrate robust yet flexible behavior, highlighting its promise for wearable energy storage. This work establishes surface-termination engineering in MXene–graphene hybrids as a promising route toward high-capacity, durable, and mechanically compliant Na–S batteries.

KEYWORDS: sodium—sulfur batteries, V_2CT_x MXene, reduced graphene oxide, chemical adsorptio, catalytic conversion, flexible cathode, first-principles calculations, surface-termination engineering

1. INTRODUCTION

Metal—sulfur cathodes are among the most promising candidates for next-generation energy storage due to their high theoretical energy density and capacity. 1,2 For example, Li—S batteries can deliver a theoretical energy density of 2600 Wh $\rm kg^{-13}$ and a capacity of 1675 mAh $\rm g^{-1},^4$ far exceeding those of conventional Li-ion batteries (155 mAh $\rm g^{-1}, 387$ Wh $\rm kg^{-1}).^5$ However, lithium-ion technology faces limitations such as high cost and restricted lithium availability, 6,7 raising concerns about long-term sustainability. 8,9

Sodium—sulfur (Na–S) batteries have emerged as a cost-effective and sustainable alternative, offering a theoretical energy density of 1274 Wh kg⁻¹ at room temperature, ¹⁰ low material cost owing to the abundance of sodium and sulfur, ^{11,12} and environmental compatibility. ^{10,13} Yet, their practical deployment is hindered by poor electrode conductivity, sluggish polysulfide (Na₂S_n) conversion, and severe polysulfide dissolution. ¹⁴ Dissolved long-chain polysulfides ($4 \le n \le 8$) shuttle to the anode, causing contamination and side reactions, ^{15,16} while short-chain species ($1 \le n \le 2$) and an ~80% volume change between S and Na₂S^{17,18} degrade structural integrity. Polar anchoring materials (AMs) such as metal oxides, sulfides,

carbides, phosphides, and borides^{19–21} have been explored to immobilize polysulfides and accelerate their conversion.

Two-dimensional MXenes—transition metal carbides, carbonitrides, and nitrides—have gained particular attention for their electrical conductivity, tunable surface chemistry, and mechanical robustness. Their inherent flexibility makes them promising for wearable and flexible energy storage. However, challenges such as oxidation, defect-induced instability, and self-restacking of nanosheets limit their performance, reducing accessible surface area and ion transport pathways. Hybridization with reduced graphene oxide (rGO) and heteroatom doping are effective strategies to mitigate restacking, enhance conductivity, and improve cycling stability. All solutions are stability.

Received: August 31, 2025 Revised: October 21, 2025 Accepted: October 26, 2025



Beyond structural modifications, *surface terminations* critically influence the MXene electrochemical behavior. Different terminations alter ion adsorption energies, diffusion barriers, and cycling stability. For instance, S-terminated Ti₃C₂ reduces Na-ion adsorption barriers by 50% compared to Oterminated surfaces, while S-terminated Ti₂C shows triple the specific capacity of pristine Ti₂C for Mg-ion intercalation. Although V₂CT_x exhibits superior cycling stability over Ti₃C₂T_x and Mo₂CT_x, the role of mixed terminations remains largely unexplored, particularly for Na—S cathodes.

Here, we address this gap by designing a mixed-terminated S/ F V₂C MXene integrated with rGO, V₂CF_{0.67}S_{0.33} (rGO), to synergistically enhance polysulfide anchoring, catalytic conversion, and mechanical flexibility. Using density functional theory (DFT), we reveal that this coterminated MXene-rGO composite achieves markedly higher polysulfide adsorption energies (0.8-3.90 eV) than single-terminated analogues, while preserving metallic conductivity for efficient electron transport. It also exhibits the lowest Na₂S decomposition barrier reported for MXene-based Na-S cathodes (0.287 eV), promoting fast sulfur utilization. Electronic structure and bonding analyses confirm strong interfacial interactions, and stress-strain simulations demonstrate robust flexibility. Our findings highlight surface-termination engineering of MXene-graphene composites as a promising pathway toward high-capacity, durable, and flexible Na-S batteries.

2. COMPUTATIONAL METHODS

2.1. DFT and Catalysis Calculations. First-principles calculations were performed using the Vienna Ab initio Simulation Package (VASP)³⁷ within the Perdew–Burke–Ernzerhof (PBE) generalized gradient approximation (GGA),³⁸ with van der Waals interactions treated via the DFT-D3 correction of Grimme.³⁹ The projector augmented wave (PAW) method⁴⁰ was used with a plane-wave cutoff of 415 eV and a 7 × 7 × 1 Monkhorst–Pack k-point mesh.⁴¹ Spin polarization was included in all calculations, and a vacuum gap of 20 Å was applied along the out-of-plane direction. Structures were relaxed until the forces on all atoms were below 0.01 eV Å⁻¹. The V₂C structures were modeled using $p(3 \times 3)$ hexagonal unit cells with a V–C–V trilayer structure (Figure S1). Optimized lattice constants deviated by \approx 0.4% from experiment and matched prior reports.³³

Surface-functionalized (S, F, and S/F coterminated) V₂C MXenes were investigated in combination with reduced graphene oxide (rGO) substrates and bare monolayer V2CS surface. A representative mixedtermination model, V2CF_{0.67}S_{0.33} (rGO), was selected based on experimental evidence indicating partial substitution of F by S terminations after etching and storage.⁴² This composition captures the essential effects of mixed terminations on catalytic behavior, while the systematic variation of F/S ratios will be explored in future work. The adsorption of Na_2S_n (n = 1, 2, 4, 6, 8) and S_8 using DFT total energies changes, Gibbs free energy changes for the sulfur reduction reaction (SRR) via vibrational frequency analysis, and Na2S decomposition barriers using the climbing-image nudged elastic band (CI-NEB) method⁴³ were calculated. Charge transfer was evaluated via Bader analysis, 44 and bonding interactions were probed with crystal orbital Hamilton population (COHP) calculations. 45 Full computational parameters, pseudopotentials, supercell specifications, convergence thresholds, and explicit adsorption/free-energy equations are given in the Supporting Information.

2.2. Mechanical Property Calculations. Mechanical stability and flexibility were evaluated through first-principles stress—strain simulations in the linear elastic regime. Elastic constants (C_{ij}) were obtained from strain—energy relationships, and the corresponding Young's modulus (Y), shear modulus (G), and Poisson's ratio (ν) were derived using standard tensor relationships for 2D hexagonal lattices. Calculations were performed in VASP, with input preparation and postprocessing via VASPKIT 1.3.1. Similar methods have been used

in previous studies to examine the mechanical stability of 2D semiconductor materials, ⁴⁷ and the results showed good agreement with available experimental and theoretical data. The complete derivations of the elastic tensor in Voigt notation, strain—energy expressions, definitions of tensile strain, and strain ranges used are detailed in the Supporting Information.

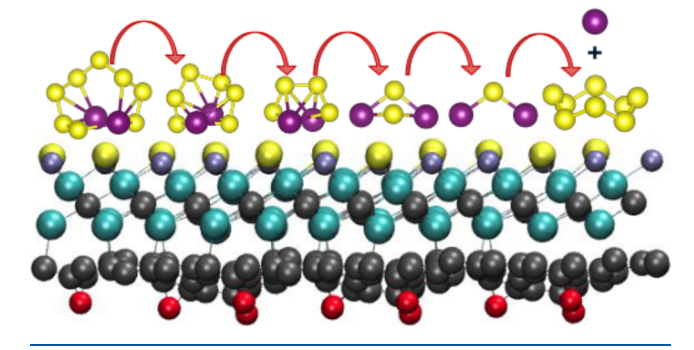
3. RESULTS AND DISCUSSION

3.1. Adsorption Mechanism of Na_2S_n on VCX. In Na-Sbatteries, the electrochemical conversion of sulfur is governed by interactions between NaPS and the catalyst surface, a process collectively termed the SRR. This reaction begins during discharge with the adsorption of S₈ molecules onto the VCX monolayer surfaces [V₂CS (bare), V₂CS (rGO), V₂CF (rGO), and V_2CFS (rGO) or $V_2CF_{0.67}S_{0.33}$ (rGO)], started calculation for subsequent reduction steps. The interaction of S₈ with Na ions leads to the formation of long-chain, soluble polysulfides such as Na₂S₈, Na₂S₆, and Na₂S₄. At this stage, a moderate binding affinity between the catalyst and these soluble intermediates is critical for anchoring them on the surface and mitigating the polysulfide shuttle effect, which otherwise results in capacity fading. As the discharge progresses, the reaction pathway advances toward forming short-chain, insoluble species such as Na₂S₂ and Na₂S. Catalysts with suitable activity can accelerate the conversion to these terminal discharge products. Conversely, during the charging process, Na2S is oxidized and gradually decomposes back to elemental sulfur (S₈), thereby completing the redox cycle. Scheme 1 illustrates the polysulfide reduction process on the V2CFS (rGO) surface, which ultimately leads to the formation of the S₈ molecule and the release of free sodium ions.

Scheme 1. Schematic Representation of the Polysulfide Reduction Mechanism on the V_2CFS (rGO) Surface

Na V OF

Polysulfide catalytic reduction



We first determined their ground-state structures in the gas phase to evaluate the adsorption behavior of various polysulfides and sulfur clusters. The most energetically favorable adsorption configurations of S_8 and Na_2S_n (n=1,2,4,6, and 8) on both bare and functionalized MXene surfaces are presented in Figure S2. The corresponding binding energies are listed in Figure 1 and Table S1. Previous studies indicate that interactions of Na_2S_n species with common electrolyte solvents such as DOL, DME, or DMSO are relatively weak (<1 eV). ^{48,49} In comparison, adsorption energies on $V_2CFS(rGO)$ are significantly stronger (2–4 eV), suggesting that solvent effects are unlikely to alter the

ACS Applied Nano Materials

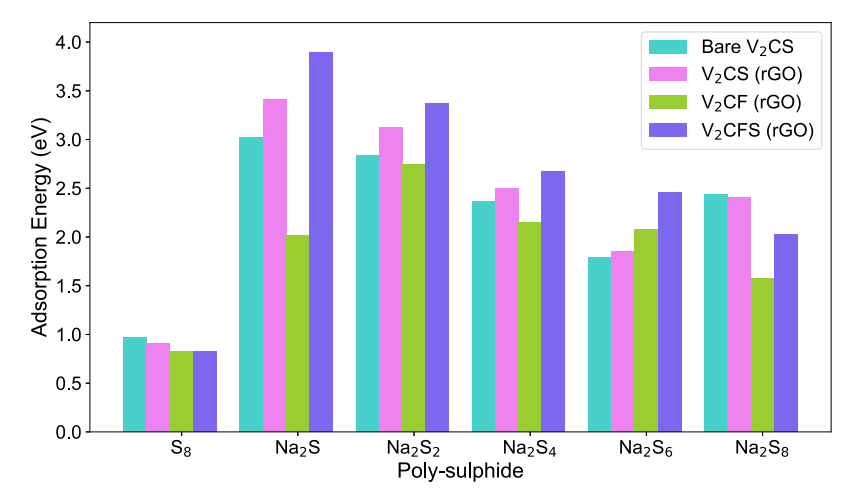


Figure 1. Calculated adsorption energies of S_8 and Na_2S_n (n = 1, 2, 4, 6, and 8) on various surfaces, including bare V_2CS and rGO-supported V_2CS , V_2CF , and V_2CFS , highlighting the influence of surface functionalization and support on adsorption strength.

adsorption trends qualitatively. Therefore, all calculations were performed in the gas phase to capture the intrinsic surface—adsorbate interactions. All sodium polysulfides (NaPS) species adopted three-dimensional cluster-like geometries upon adsorption, which is consistent with the structural features previously reported for lithium polysulfides and further supported by earlier studies on sodium-based analogs. Multiple initial configurations with varied orientations (vertical, tilted, and parallel) and adsorption sites (top, bridge, and hollow) were tested for each Na_2S_n species. All optimizations consistently converged to the same adsorption motif, with Na atoms oriented toward surface terminations, confirming that the reported structures represent the most stable configurations.

As shown in Table 1, the minimum distance between the S_8 molecule and various catalytic surfaces ranges from 3.08 to 3.84

Table 1. Minimum Distances (in Å) between Atoms in Adsorbed Polysulfide Species and the Catalyst Surface Indicate the Nature and Strength of Surface—Absorbate Interactions across Different Anchoring Materials

surfaces	$\begin{pmatrix} S_8 \\ (S-S) \end{pmatrix}$	Na_2S_8 (Na-S)	Na_2S_6 (Na-S)	Na_2S_4 (Na-S)	Na_2S_2 (Na-S)	Na ₂ S (S-S)
V ₂ CS (bare)	3.60	2.91	2.75	2.76	2.64	2.04
V_2CS (rGO)	3.38	2.87	2.77	2.81	2.75	2.04
V_2CF (rGO)	3.08	2.39	2.36	2.34	2.28	2.34
V ₂ CFS (rGO)	3.84	2.27	2.32	2.25	2.28	2.07

Å, accompanied by adsorption energies between 0.969 and 0.823 eV (see Figure 1 and Table S1). These values and Figure S2 indicate that the S_8 molecule adsorbs onto the surfaces in a parallel orientation, predominantly stabilized by van der Waals interactions, with no evidence of chemical bond formation. This mode of interaction aligns with previous reports on other anchoring materials, where similar parallel adsorption configurations of S_8 have been observed. Furthermore, the puckered ring geometry of the S_8 molecule and the structural integrity of the AM surfaces remain largely preserved following adsorption, suggesting minimal perturbation upon binding.

In contrast, sodium polysulfides (Na_2S_n , with n = 8, 6, 4, 2, 1) display stronger interactions with the surfaces. These species generally adopt configurations in which their Na atoms are oriented toward the substrate, facilitating the formation of Na–S bonds. Notably, Na_2S exhibits a distinct adsorption mode,

wherein the Na atoms occupy hollow sites of the termination layer, while the S atom resides directly above a surface termination atom. With these configurations, all three atoms form covalent bonds with the substrate termination atoms, except in the case of V_2CF (rGO). Despite forming surface bonds, the Na_2S_n species maintain their molecular integrity across all surfaces, with only slight structural distortions observed postadsorption (see Figure S2). The preservation of molecular rigidity without dissociation is critical for the reversibility of the redox processes in Na–S batteries.

A general decreasing trend of the Na–S bond lengths is observed across the series of adsorbed Na₂S_n species (Table 1), with the shortest bond length occurring for Na₂S. As the reduction progresses, this trend signifies increasingly stronger interactions between the AM surfaces and the polysulfide species. Moreover, as illustrated in Figure 1, Na₂S_n species (n = 1, 2, 4, 6) exhibit the most substantial adsorption on the mixed F- and S-terminated surfaces, evidenced by both higher adsorption energies and shorter bond distances relative to bare, singly S-terminated, or F-terminated surfaces. This enhanced interaction suggests that mixed terminations provide the most favorable environment for anchoring polysulfides, offering an effective strategy to suppress the polysulfide shuttle

3.2. Catalytic Conversion of Polysulfide Clusters. One of the primary challenges in sodium—sulfur batteries is the inherently sluggish redox kinetics, which, when combined with the prolonged presence of Na_2S_n species in the electrolyte, exacerbates the shuttle effect. To address this issue, we systematically investigated how different surface terminations influence the catalytic activity of the electrode and facilitate the reversible electrochemical steps of the SRR. During the discharge process, the SRR involves a series of transformations, ultimately forming Na_2S from elemental sulfur (S_8) and sodium metal. This multistep reaction pathway includes several polysulfide intermediates, as reported in previous studies. So,48 Overall, the complete discharge of a Na-S battery involves a total transfer of 16 electrons, culminating in the production of eight Na_2S molecules. Detailed steps are summarized in Section

The complete evolution profile from S_8 to Na_2S is depicted in Figure 2, highlighting the stepwise free energy changes associated with the SRR across different catalytic surfaces. The

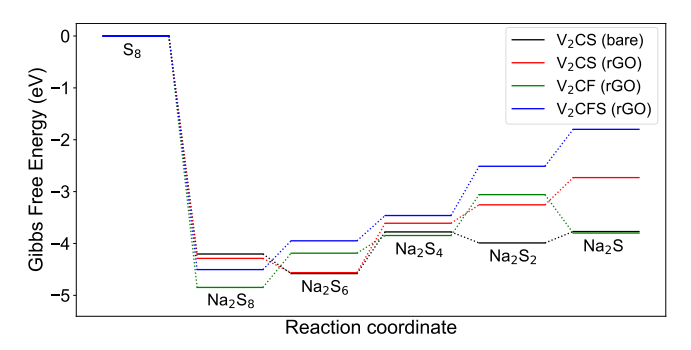


Figure 2. Gibbs free energy profiles of the sulfur reduction reaction during discharge on various V_2C -based catalytic surfaces, illustrating the thermodynamic feasibility and reaction energetics at each intermediate step.

first step, the reduction of S₈ to Na₂S₈, is found to be spontaneously exothermic on all surfaces, releasing the highest amount of energy ($\Delta G_1 = -4.847 \text{ eV}$) on the V₂CF (rGO) surface. This strongly exergonic initial step suggests a favorable onset for SRR, especially on fluorine-functionalized systems. In contrast, the second step (ΔG_2) , corresponding to the conversion of Na₂S₈ to Na₂S₆, exhibits apparent surfacedependent behavior. It is endothermic on V2CF (rGO) and V₂CFS (rGO), requiring 0.660 and 0.555 eV, respectively. However, this same step is exothermic on the bare and V₂CS (rGO) surfaces, with energy releases of -0.377 and -0.275 eV, respectively. This indicates that bare and sulfur-terminated surfaces may stabilize intermediate polysulfides more efficiently during this transition. The third step (ΔG_3) , involving the conversion to Na₂S₄, is endothermic across all surfaces; nonetheless, V2CF (rGO) requires the least energy input (0.340 eV), reflecting its relatively low thermodynamic barrier for this stage. The fourth step (ΔG_4), which corresponds to the formation of Na₂S₂, is energetically favorable only on the V₂CS (bare) surface (-0.212 eV), whereas the same transformation remains endothermic on the other three surfaces, suggesting a specific affinity of the bare surface for this intermediate. The final step (ΔG_5) , which represents the crucial solid-to-solid conversion from Na₂S₂ to Na₂S, is significantly endothermic on V₂CS (bare), V₂CS (rGO), and V₂CFS (rGO), with energy requirements of 0.220, 0.525, and 0.712 eV, respectively. In sharp contrast, this step is exothermic on the V₂CF (rGO) surface (-0.740 eV), indicating strong catalytic promotion of this final conversion on the fluorine-functionalized MXene. Overall, the V₂CF (rGO) surface consistently exhibits lower energy barriers for several key steps and notably promotes the terminal conversion to Na₂S, effectively overcoming the thermodynamic bottlenecks typical of SRR. While all of the studied surfaces facilitate the S_8 to Na_2S conversion with an overall exothermic energy profile, the V₂CF (rGO) system stands out in enhancing the thermodynamics of the redox process, thereby offering a promising route to mitigate the sluggish reaction behavior inherent in Na-S batteries.

3.3. Dissociation Mechanism of Na₂S. The reversibility and operational lifespan of sodium-sulfur batteries are critically governed by the catalytic decomposition barrier of the solid redox intermediate Na₂S, which is the final discharge product in the electrochemical cycle. 52 As Na₂S remains insoluble mainly in the electrolyte during both charge and discharge, its efficient decomposition is essential to sustain redox reversibility. For improved reaction kinetics, a low dissociation barrier is highly desirable. During the charging process, Na2S undergoes bond cleavage to release sulfur, eventually reforming the elemental cyclo- S_8 . This transformation proceeds via the reaction $Na_2S \rightarrow$ $NaS + Na^{+} + e^{-,53}$ where the liberated Na^{+} ions subsequently migrate across the catalytic surface (VCX) along energetically favorable pathways. This decomposition process entails overcoming two key energetic requirements: (i) breaking the Na-S bond at the initial adsorption site and (ii) enabling the diffusion of Na⁺ ions to adjacent secondary adsorption sites. This mechanistic pathway is illustrated in Figure 3. Notably, prior experimental investigations have shown that a high decomposition energy barrier can substantially suppress the cell voltage,⁵⁴ underscoring the importance of efficient Na₂S dissociation for maintaining optimal battery performance.

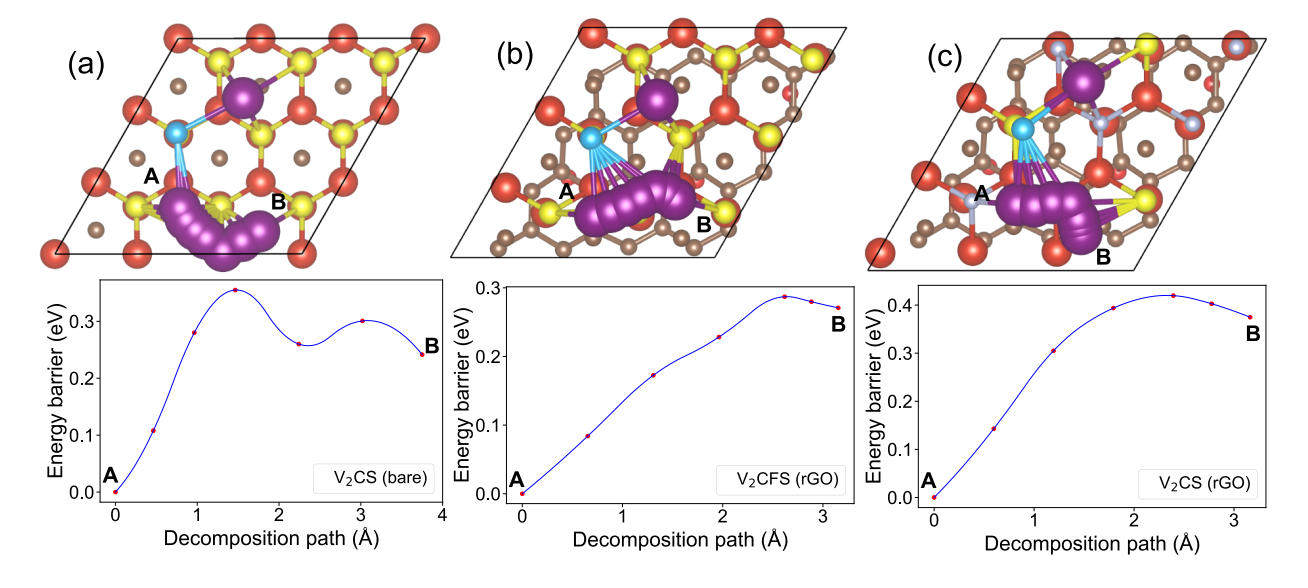


Figure 3. Decomposition energy barriers of Na_2S on (a) V_2CS (bare), (b) V_2CS (rGO), and (c) V_2CFS (rGO) surfaces. Here, the V_2CF (rGO) surface does not show Na_2S decomposition. The top panels depict the reaction pathway involving Na-S bond cleavage and subsequent Na^+ ion migration across the surface. The bottom panels show the corresponding CI-NEB-calculated energy profiles, highlighting the decomposition barriers on each catalytic surface. Color scheme of atoms: V—red; C—brown; S (from AM)—yellow; F—silver; S (from S)—sky blue.

ACS Applied Nano Materials www.acsanm.org Article

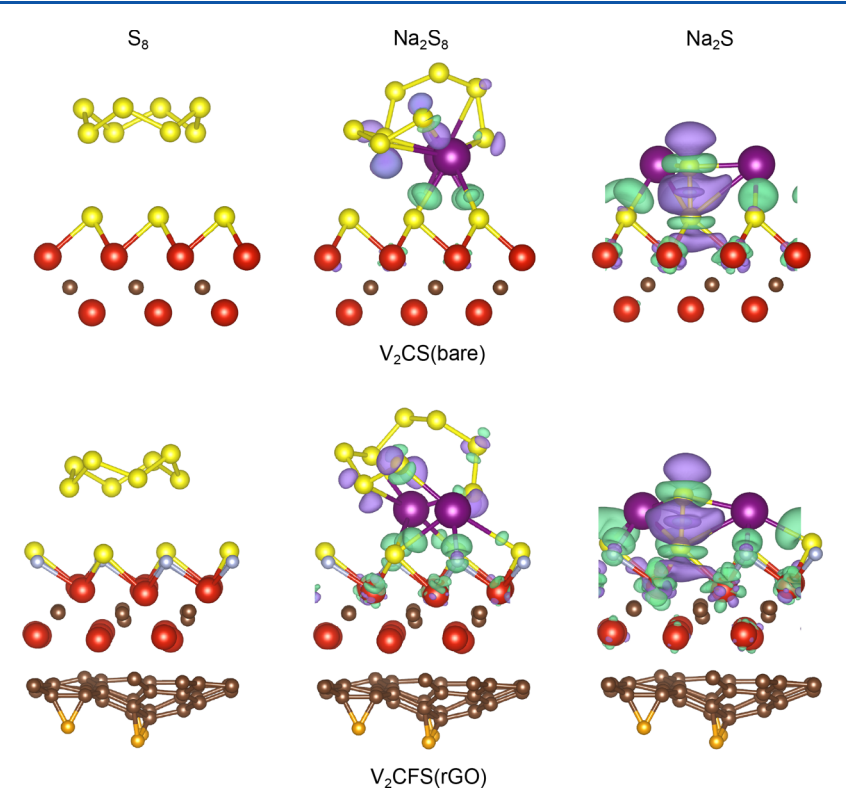


Figure 4. Isosurface plots illustrate charge density differences upon adsorption, with the top panels showing the V_2CS (bare) surface and the bottom panels showing the V_2CFS (rGO) surface. Green and purple regions represent electron accumulation and depletion at an isosurface value of 0.0031 e/ \mathring{A}^3 . Color scheme of atoms: V, red; C, brown; S, yellow; F, silver; Na, purple; O, orange.

Therefore, both the Na₂S dissociation energy barrier and the underlying ionic diffusion landscape play pivotal roles in determining the electrochemical efficiency of Na–S batteries.

To gain insights into this critical step, we employed the climbing-image nudged elastic band method⁴³ to evaluate the Na₂S decomposition energy barriers on various catalytic surfaces. As shown in Figure 3, the energy barrier for Na₂S dissociation is remarkably low on the V₂CS (bare) and V₂CS (rGO) surfaces—0.355 and 0.419 eV, respectively—representing a dramatic reduction compared to the barrier in the gas phase (2.199 eV; see Figure S3). Interestingly, among all anchoring materials, V₂CFS (rGO) exhibits the lowest decomposition energy barrier of 0.287 eV (Figure 3c), indicating highly favorable catalytic activity for promoting Na-S bond cleavage. In contrast, the V₂CF (rGO) surface fails to facilitate Na₂S dissociation, emphasizing that dual surface terminations (F and S) are crucial for activating this key transformation. This behavior can be attributed to the weak interaction between the sulfur atom in Na₂S and the V₂CF (rGO) surface, as illustrated in Figure S2. Because no stable bond is formed, the adsorption energy remains relatively low (Table S1), making the dissociation of Na-S bonds energetically unfavorable. As a result, Na₂S tends to remain intact and undissociated. The origin of this weak dissociation pathway is further clarified by the COHP analysis presented in the next section.

Although V₂CFS (rGO) exhibits an endothermic free energy change in the final step ($\Delta G_5 = 0.712 \text{ eV}$), the overall catalytic process remains favorable when both thermodynamics and kinetics are considered. Notably, V₂CFS (rGO) shows the lowest Na₂S decomposition barrier (0.287 eV, Figure 3), enabling a faster regeneration of active sites. In contrast, V₂CF (rGO)—despite its strongly exothermic initial step—does not

effectively facilitate Na₂S dissociation. These results highlight that mixed terminations promote balanced adsorption and superior catalytic activity compared to a single F-termination.

3.4. Electron Density and Bond Interaction Analysis. Among the studied surfaces, mixed-terminated V_2CFS (rGO) emerged as the most promising Na–S cathode material due to its lowest catalytic decomposition barrier. To gain deeper insight into the decomposition mechanisms of S_8 and Na_2S_n species ($n=8,\ 1$) and the associated Na–S and S–S bonding after adsorption, we conducted electronic structure analyses on V_2CFS (rGO) and compared them with bare V_2CS . These included charge density difference, partial density of states (PDOS), and COHP calculations, which together reveal the chemical bonding characteristics between S_8 , Na_2S_8 , and Na_2S and the catalyst surfaces.

We conducted Bader charge analysis to evaluate the extent of charge transfer during adsorption. The results indicate that the nonsodiated S₈ species exhibit weak interactions with both V₂CS (bare) and V₂CFS (rGO) surfaces, with minimal charge transfers of only 0.003 and 0.006 lel, respectively. This limited transfer is primarily attributed to weak S-S interactions. As the discharge process progresses, a greater number of electrons is transferred from Na₂S_n species to the substrate, reflecting stronger interfacial interactions. Specifically, the adsorption of Na₂S₈ and Na₂S results in significant net charge gains on the V_2CS (bare) surface (-0.680 and -1.106 lel) and even higher gains on the V_2 CFS (rGO) surface (-0.806 and -1.159 lel), respectively. These results clearly indicate that the V₂CFS (rGO) surface enables a more efficient charge transfer, underscoring its enhanced catalytic activity. The charge transfer distributions for S₈, Na₂S₈, and Na₂S adsorbed on both V₂CS (bare) and V₂CFS (rGO) are visualized in Figure 4.

ACS Applied Nano Materials www.acsanm.org Article

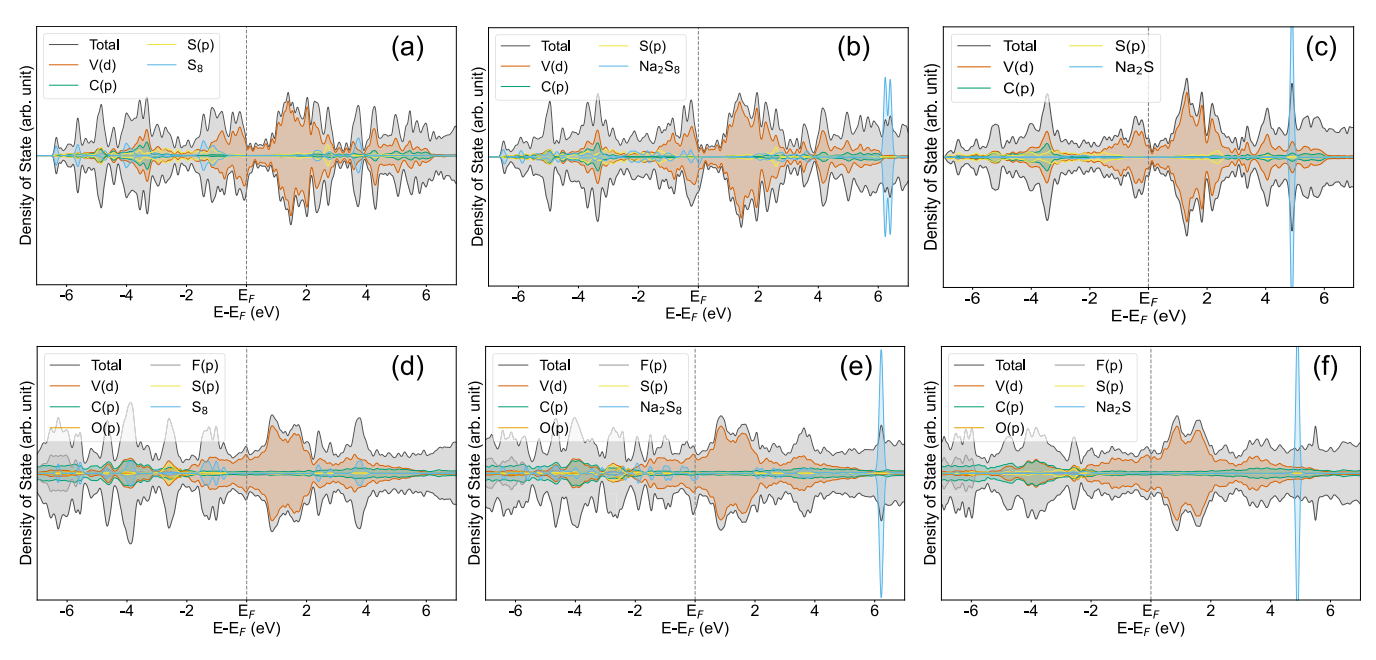


Figure 5. Projected density of states of polysulfides adsorbed on catalytic surfaces. Panels (a-c) show PDOS for S_8 , Na_2S_8 , and Na_2S adsorbed on V_2CS (bare), respectively, while panels (d-f) show the corresponding PDOS for the same species adsorbed on V_2CFS (rGO). The DOS for the pristine systems is shown in Figure S5.

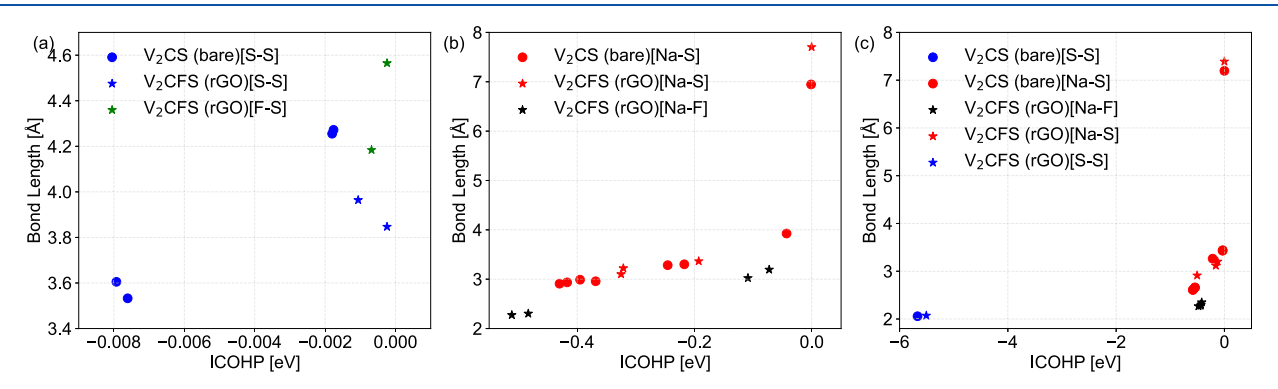


Figure 6. Correlation between the ICOHP values and the interatomic distances for the interactions of polysulfide species—(a) S_8 , (b) Na_2S_8 , and (c) Na_2S —and the $V_2CS(bare)/V_2CFS(rGO)$ surfaces. Atomic pairs considered (listed in parentheses) are color-coded as follows: S–S (blue), F–S (green), Na–S (red), and Na–F (black).

Furthermore, the corresponding charge density differences along the *z*-axis, presented in Figure S4, offer an additional visual confirmation of these findings.

The inherently low electronic conductivity of elemental sulfur (S₈) and the intermediate sodium polysulfides formed during the charge/discharge cycles pose a significant challenge to the electrochemical performance of Na-S batteries. This limitation significantly impedes the redox kinetics. In contrast, conductive catalytic surfaces that facilitate electron transfer during redox reactions involving Na_2S_n species can substantially enhance the reaction kinetics. To explore the electronic behavior of such catalytic substrates, we investigated the density of states (DOS) of V₂CS (bare) and V₂CFS (rGO) during the adsorption of S₈ and Na_2S_n species. The projected density of states and total density of states (TDOS), shown in Figure 5a-f, clearly demonstrate that both surfaces exhibit metallic characteristics. Notably, the TDOS comparison before and after the adsorption of S_8/Na_2S_n (n = 8, 1), illustrated in Figures S5 and 5, respectively, confirm that the metallic nature of V₂CS (bare) and V₂CFS (rGO) is retained even after the adsorption of polysulfide species. This preservation of metallicity highlights

the potential of these surfaces to support efficient electron transport during electrochemical processes in Na–S batteries.

In pristine V_2CS (bare), a high density of states at the Fermi level confirms its intrinsic metallic character and good electronic conductivity (Figure S5). Hybridization with reduced graphene oxide further increases this density, while fluorine and mixed fluorine—sulfur terminations enhance it even more, providing additional states for charge transport. These features align with the stronger adsorption energies and improved catalytic activity observed in the SRR. Adsorption of nonsodiated S_8 (Figure 5) induces only minor changes to the electronic structure, with the Fermi level dominated by states from the catalytic substrates, consistent with its weak binding and minimal charge transfer.

By contrast, Na_2S_8 adsorption introduces additional states near the Fermi level, originating mainly from S-p and Na-s orbitals, indicating charge transfer to the substrate and correlating with its higher adsorption energy. For Na_2S , the Na-s states shift closer to the Fermi level, further facilitating electron transfer. Notably, the emergence of new states near the Fermi level upon Na_2S_8 adsorption strengthens the electronic coupling between the polysulfide species and the substrate.

ACS Applied Nano Materials www.acsanm.org Article

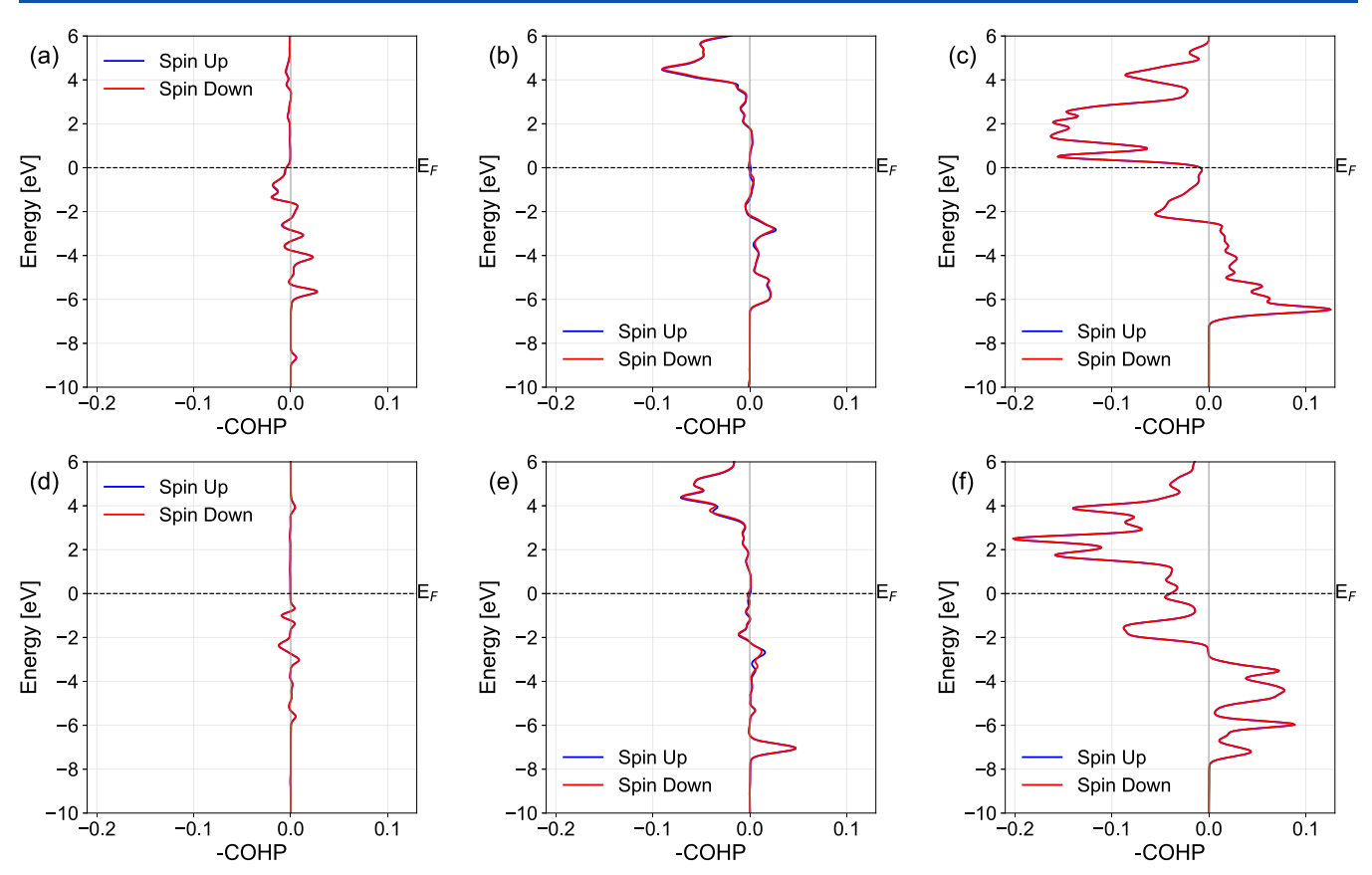


Figure 7. Averaged -COHP plots represent key interactions between the adsorbed species and the catalytic surfaces. Panels (a-c) show interactions for S_8 , Na_2S_8 , and Na_2S on the V_2CS (bare) surface, while panels (d-f) depict the corresponding interactions on the V_2CFS (rGO) surface. The horizontal dashed line at zero marks the Fermi level (E_F) .

These states facilitate efficient electron injection into Na–S bonds, thereby reducing the decomposition barrier and accelerating the redox kinetics. This interpretation aligns with the charge-density-difference and Bader analyses, which reveal significant charge transfer and electron localization around Na–S bonds, particularly for the V₂CFS(rGO) surface. In all cases, V 3d states of the substrates dominate the upper valence band region, and both V₂CS (bare) and V₂CFS (rGO) retain their metallicity after adsorption, supporting their role as efficient electron-conducting channels during redox transformations. Additional discussions are provided in Section S3.

To further elucidate the bonding between S_8/Na_2S_n (n=8,1) and V_2CS (bare)/ V_2CFS (rGO), we performed a COHP analysis on the Na–S valence orbitals (Figures 6 and 7). While DOS reveals the distribution of electronic states, COHP decomposes them into bonding, antibonding, and nonbonding contributions based on Hamiltonian matrix elements. Positive –COHP values denote bonding, negative values indicate antibonding, and values near zero correspond to nonbonding interactions. The integrated COHP (ICOHP) up to the Fermi level provides a quantitative measure of bond strength, with more negative values indicating stronger interactions.

The relationship between the ICOHP and bond lengths is shown in Figure 6. For nonsodiated S_8 , the S-3p orbitals of both catalytic surfaces exhibit weak interactions with the S-3p orbitals of the adsorbate, reflected in small ICOHP values—ranging from -0.00180 to -0.00793 eV/bond for V_2 CS (bare) and from -0.00024 to -0.00106 eV/bond for V_2 CFS(rGO). The interaction between the F-2p orbitals of V_2 CFS(rGO) and the S-3p orbitals of S_8 is even weaker, confirming the

physisorptive nature of this interaction. Quantitative %-COHP partitioning shows that S-S and F-S interactions contribute 58.6 and 41.4% of the total bonding, respectively, indicating that while S-S bonds dominate, F-S bonds provide meaningful secondary stabilization at the interface.

For Na_2S_8 adsorption, larger ICOHP values associated with Na–S bonds (-0.00115 to -0.42998 eV/bond on V_2CS and -0.00024 to -0.32516 eV/bond on $V_2CFS(rGO)$) confirm stronger chemical interactions. Additionally, $V_2CFS(rGO)$ exhibits appreciable Na–F bonding (-0.07261 to -0.51138 eV/bond), demonstrating the involvement of fluorine in interfacial stabilization. The %-COHP partitioning indicates that Na–S and Na–F bonds contribute 41.6 and 58.4% of the total interfacial bonding, respectively, underscoring the cooperative role of mixed terminations in modulating interaction strength.

The strongest interactions occur for Na_2S adsorption, where Na-3s and S-3p orbitals form robust bonds on both surfaces, with ICOHP values ranging from -0.00076 to -0.58354 eV/bond for V_2CS and -0.00108 to -0.50433 eV/bond for $V_2CFS(rGO)$. The S-S bonds at the Na_2S -surface interface exhibit the highest ICOHP values (-5.66829 and -5.50632 eV/bond for V_2CS and $V_2CFS(rGO)$, respectively). The corresponding %-COHP partitioning shows that Na-S, Na-F, and S-S bonds contribute 9.8, 22.0, and 68.2% of the total interfacial bonding, respectively, confirming that F-containing bonds, while secondary, significantly enhance interfacial stability.

Overall, the quantitative %-COHP analysis demonstrates that although S—S bonds dominate interfacial interactions, introducing F-containing terminations provides moderate bonding

contributions that stabilize the interface without causing overbinding. This balanced interaction strength supports efficient catalytic turnover, which is consistent with the Sabatier principle. The results highlight the importance of mixed terminations in promoting both structural stability and catalytic efficiency for polysulfide conversion on MXene-based electrodes.

The average -COHP plots presented in Figure 7b,e for Na₂S₈ and Figure 7c,f for Na₂S reveal prominent antibonding states. When these COHP profiles are compared with the corresponding ICOHP values, the observed antibonding peaks can be attributed to charge transfer from the Na-3s orbitals to the highenergy unoccupied S-3p orbitals in V_2 CS, as well as to the S-3p and F-2p orbitals in V₂CFS (rGO). Furthermore, Figure 7f highlights a notably larger presence of antibonding orbitals near the Fermi level on the V₂CFS (rGO) surface compared to V₂CS (bare) in the Na₂S-adsorbed phase (Figure 7c). This increased antibonding character near the Fermi level suggests enhanced charge transfer dynamics between Na₂S and the V₂CFS (rGO) substrate. The Bader charge analysis further supports such an interpretation, which quantitatively confirms greater electron transfer in the case of V₂CFS (rGO), thereby reinforcing the role of fluorinated surfaces in improving charge mediation and catalytic behavior.

The dissociation behavior of Na_2S on different surfaces can be rationalized through ICOHP analysis. For the Na-S bonds within Na_2S , the ICOHP value is ≈ -1.12 eV/bond, reflecting a strong internal stabilization that is energetically costly to break. On the F-terminated V_2C surface, the Na_2S –surface interaction is negligible (-0.016 eV/bond), far weaker than the internal Na-S bonding. As a result, the surface cannot compensate for the loss of internal stabilization, leaving Na_2S intact. In contrast, for bare V_2CS , the Na_2S –surface ICOHP is much stronger (-5.67 eV/bond) and remains comparably strong for the mixed S/F termination (-5.50 eV/bond). These values are significantly more negative than the internal Na-S bond, indicating that surface bonding can offset the cost of breaking Na-S interactions and thereby promote sulfur dissociation.

Comparable trends have been reported in previous studies,⁵⁸ where DFT-predicted strong polysulfide adsorption on MXenes such as $V_4C_3T_x$ was later validated experimentally through visual polysulfide sequestration and diffusion tests, confirming effective suppression of the shuttle effect via combined physical confinement and chemical anchoring. Given the close structural and electronic resemblance between V₄C₃T_x and the present V₂CFS(rGO) system, a similar correspondence between theoretical predictions and experimental observations can be reasonably anticipated. This consistency underscores the reliability of our computational findings and their relevance to practical Na-S battery applications. To comparatively benchmark the present work with previously reported MXene-based cathodes (as shown in Table S2), this confirms the lowest decomposition barrier and strong binding of Na₂S on V₂CFS (rGO), helping to improve its catalytic activity and facilitate efficient polysulfide conversion.

While the present study focuses on theoretical insights into the interfacial and electronic mechanisms governing polysulfide conversion, experimental validation through cycling stability and rate capability measurements remains an important next step. The computational findings presented here are expected to guide future experimental efforts toward realizing and evaluating $V_2 \mbox{CFS}(r\mbox{GO})\mbox{-based}$ cathodes in practical Na–S battery systems.

3.5. Mechanical Stability of V_2CS (Bare) and V_2CFS (rGO) Layer. To evaluate the suitability of the material for flexible applications, it is essential to understand its mechanical properties. The relationships between the elastic constants and mechanical moduli were determined by using the stress—strain method. A summary of the calculated mechanical properties is outlined in Table 2. It can be observed that both V_2CS (bare)

Table 2. Calculated Mechanical Properties of V_2CS (Bare) and V_2CFS (rGO) Composites, Including Elastic Constants (C_{11}, C_{12}) , Young's Modulus (Y), and Shear Modulus (G), Highlighting Their Structural Stability and Mechanical Flexibility

property	V ₂ CS (bare)	V ₂ CFS (rGO)
Young's modulus (Y) (N/m)	143.036	218.782
shear modulus (G) (N/m)	55.102	105.799
Poisson's ratio, ν	0.298	0.034
elastic constants, C_{ij} (N/m)	$\begin{pmatrix} C_{11} = 156.968 \\ C_{12} = 46.763 \end{pmatrix}$	$\begin{pmatrix} C_{11} = 219.035 \\ C_{12} = 7.437 \end{pmatrix}$

and V₂CFS (rGO) satisfy the Born criteria for elastic stability, ⁵⁹ which can be defined as $C_{11} > 0$ and $C_{11} > |C_{12}|$. Young's modulus has been previously reported to range from 380 to 470 GPa for ordered graphene oxides, depending on the degree of oxygen functional group coverage. ⁶⁰

The calculated Young's modulus of the V₂CFS (rGO) composite is 218.78 N/m, which is slightly lower than the experimentally reported values for monolayer Ti₃C₂T_r (318 N/ m) and graphene (335 N/m).⁶¹ This moderate reduction in stiffness indicates enhanced mechanical flexibility, making the composite a promising candidate for use in flexible cathodes. While the incorporation of rGO into the MXene matrix improves electronic properties and interfacial interactions compared to the bare V₂CS system, the synergistic combination with functionalized MXene reduces rigidity relative to standalone rGO. This balance of moderate stiffness (Y \sim 219 N/m) and low shear resistance ($G \sim 106 \text{ N/m}$) positions V₂CFS (rGO) as a promising candidate for flexible electronics, where mechanical compliance must coexist with robust electronic performance. Moreover, despite the increase in modulus compared to that of bare V₂CS (143.036 N/m), the composite remains considerably more flexible than pristine rGO, confirming the mechanical advantage conferred by MXene integration. The elastic stability of the material, reflected in the condition $C_{11} \gg |C_{12}|$, further ensures its structural integrity under deformation—an essential characteristic for nextgeneration flexible and wearable device platforms.

Moreover, a dry anhydrous etching strategy was recently proposed to synthesize fluorine-rich and hydroxyl-free ${\rm Ti_3C_2T_x}$ MXenes. Similarly, a dry molten salt method employing sulfur substitution has been demonstrated for the synthesis of ${\rm Ti_3C_2T_x}$, effectively eliminating the need for harsh acid treatments and complex procedures. This strategy could be adapted to synthesize the proposed ${\rm V_2CT_x}$ MXenes. Moreover, the synthesis of MXene–rGO (reduced graphene oxide) composites can be carried out using freeze-drying or vacuum filtration methods, followed by thermal annealing if necessary, as demonstrated in previous studies, 44–66 which supporting the experimental feasibility of the materials proposed in this work. Despite their promise, MXenes face practical challenges related to oxidation and long-term durability. ${\rm V_2CT_x}$ is susceptible to air and aqueous oxidation, which can degrade its layered

structure and compromise stability. Nevertheless, strategies such as composite formation with conductive carbon frameworks, surface modification, or doping to strengthen polysulfide anchoring and pillared or hierarchical architectures have been shown to mitigate these issues. ^{69,70} Implementing these approaches may help unlock the full potential and practical applications of V₂CT_x for durable Na–S battery applications.

4. CONCLUSIONS

We have demonstrated that sulfur/fluorine coterminated MXene composites integrated with reduced graphene oxide—specifically $V_2CF_{0.67}S_{0.33}$ (rGO)—offer a powerful platform for high-performance, flexible room-temperature Na–S batteries. First-principles calculations reveal that this mixed-termination design markedly strengthens polysulfide anchoring, achieving adsorption energies of 0.8–3.90 eV, while preserving structural integrity and metallic conductivity for efficient electron transport.

The V₂CFS (rGO) composite exhibits the lowest Na₂S decomposition barrier reported for MXene-based Na–S cathodes (0.287 eV) and a thermodynamically favorable sulfur reduction pathway, enabling faster and more complete sulfur utilization. Electronic structure analyses (charge density difference, PDOS, and COHP) confirm that its superior performance arises from strong interfacial chemical bonding and substantial charge transfer with Na₂S_n species. Stress–strain simulations further demonstrate mechanical robustness combined with flexibility, underscoring its potential for a wearable energy storage devices.

These findings establish surface-termination engineering of MXene-graphene composites as a general strategy for suppressing polysulfide shuttling, enhancing redox kinetics, and delivering high-capacity, durable, and flexible Na-S batteries, with broader applicability to other metal-sulfur electrochemical systems.

ASSOCIATED CONTENT

Data Availability Statement

The data that support the findings of this study are available from the corresponding authors upon reasonable request.

Supporting Information

The Supporting Information is available free of charge at https://pubs.acs.org/doi/10.1021/acsanm.5c04042.

Additional computational details, the structure of V₂C monolayer, optimized geometries of Na₂S_n species adsorbed on V₂CT_x surface, decomposition energy barrier, charge density difference plots, total and partial DOS, and computed adsorption energies (PDF)

Atomic coordinates of individual species and surface configurations provided in a separate compressed file in POSCAR format (ZIP)

AUTHOR INFORMATION

Corresponding Authors

Ram Sewak – Department of Chemistry, Indian Institute of Technology Gandhinagar, Gandhinagar, Gujarat 382355, India; occid.org/0000-0001-5700-0122;

Email: ram.sewak@iitgn.ac.in

Anirban Mondal — Department of Chemistry, Indian Institute of Technology Gandhinagar, Gandhinagar, Gujarat 382355, India; o orcid.org/0000-0003-3029-8840;

ī

Email: amondal@iitgn.ac.in

Complete contact information is available at: https://pubs.acs.org/10.1021/acsanm.5c04042

Author Contributions

R.S. and A.M. conceived the research idea. R.S. performed all simulations. R.S. and A.M. analyzed the data and interpreted the results. R.S. and A.M. cowrote and revised the manuscript.

Note:

The authors declare no competing financial interest.

ACKNOWLEDGMENTS

The authors gratefully acknowledge the Indian Institute of Technology Gandhinagar, India, for providing research facilities and financial support. We thank PARAM Ananta for computational resources.

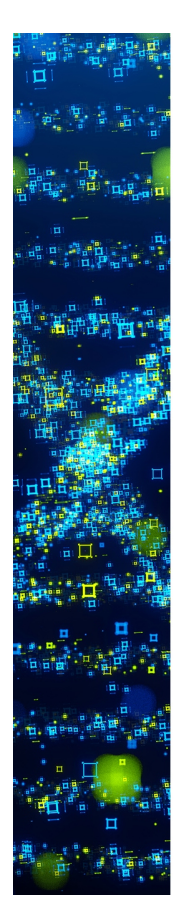
REFERENCES

- (1) Zhao, J.; Xiao, Y.-Y.; Liu, Q.; Wu, J.; Jiang, Z.-C.; Zeng, H. The Rise of Multivalent Metal—Sulfur Batteries: Advances, Challenges, and Opportunities. *Adv. Funct. Mater.* **2024**, *34*, No. 2405358.
- (2) Yao, W.; Liao, K.; Lai, T.; Sul, H.; Manthiram, A. Rechargeable Metal-Sulfur Batteries: Key Materials to Mechanisms. *Chem. Rev.* **2024**, 124, 4935–5118.
- (3) Yin, Y.-X.; Xin, S.; Guo, Y.-G.; Wan, L.-J. Lithium—Sulfur Batteries: Electrochemistry, Materials, and Prospects. *Angew. Chem., Int. Ed.* **2013**, *52*, 13186–13200.
- (4) Ji, X.; Lee, K. T.; Nazar, L. F. A highly ordered nanostructured carbon–sulphur cathode for lithium–sulphur batteries. *Nat. Mater.* **2009**, *8*, 500–506.
- (5) Barghamadi, M.; Kapoor, A.; Wen, C. A Review on Li-S Batteries as a High Efficiency Rechargeable Lithium Battery. *J. Electrochem. Soc.* **2013**, *160*, A1256.
- (6) Evarts, E. C. Lithium batteries: To the limits of lithium. *Nature* **2015**, 526, S93–S95.
- (7) Egbue, O.; Long, S.; Kim, S. D. Resource Availability and Implications for the Development of Plug-In Electric Vehicles. *Sustainability* **2022**, *14*, 1665.
- (8) Vega-Muratalla, V. O.; Ramírez-Márquez, C.; Lira-Barragán, L. F.; Ponce-Ortega, J. M. Review of Lithium as a Strategic Resource for Electric Vehicle Battery Production: Availability, Extraction, and Future Prospects. *Resources* **2024**, *13*, 148.
- (9) Innocenti, A.; Bresser, D.; Garche, J.; Passerini, S. A critical discussion of the current availability of lithium and zinc for use in batteries. *Nat. Commun.* **2024**, *15*, 4068.
- (10) Xu, X.; Zhou, D.; Qin, X.; Lin, K.; Kang, F.; Li, B.; Shanmukaraj, D.; Rojo, T.; Armand, M.; Wang, G. A room-temperature sodium—sulfur battery with high capacity and stable cycling performance. *Nat. Commun.* **2018**, *9*, 3870.
- (11) Haynes, W. M., Ed.; CRC Handbook of Chemistry and Physics, 95th ed.; CRC Press/Taylor and Francis: Boca Raton, FL, 2015; Internet Version 2015 (accessed Dec, 2014).
- (12) Torres, M. E. S.; Morales, A. R.; Peralta, A. S.; Kroneck, P. M. H. In *Transition Metals and Sulfur A Strong Relationship for Life*; Torres, M. S.; Kroneck, P., Eds.; De Gruyter: Berlin, Boston, 2020; pp 19–50.
- (13) Liang, Y.; Zhang, B.; Shi, Y.; Jiang, R.; Zhang, H. Research on Wide-Temperature Rechargeable Sodium-Sulfur Batteries: Features. *Challenges and Solutions. Materials* **2023**, *16*, 4263.
- (14) Zhang, Q.; Bo, L.; Li, H.; Shen, L.; Li, J.; Li, T.; Xiao, Y.; Tian, Z.; Li, Z. Inhibiting Shuttle Effect and Dendrite Growth in Sodium—Sulfur Batteries Enabled by Applying External Acoustic Field. *Nano Lett.* **2024**, 24, 10711–10717.
- (15) Yan, Z.; Zhao, L.; Wang, Y.; Zhu, Z.; Chou, S.-L. The Future for Room-Temperature Sodium—Sulfur Batteries: From Persisting Issues to Promising Solutions and Practical Applications. *Adv. Funct. Mater.* **2022**, 32, No. 2205622.
- (16) Wang, Y.-X.; Zhang, B.; Lai, W.; Xu, Y.; Chou, S.-L.; Liu, H.-K.; Dou, S.-X. Room-Temperature Sodium-Sulfur Batteries: A Compre-

- hensive Review on Research Progress and Cell Chemistry. Adv. Energy Mater. 2017, 7, No. 1602829.
- (17) Qi, Y.; Xu, M. Engineering towards stable sodium metal anodes in room temperature sodium-sulfur batteries: challenges, progress and perspectives. *Energy Storage Mater.* **2024**, 72, No. 103704.
- (18) Qiang, Z.; Chen, Y.-M.; Xia, Y.; Liang, W.; Zhu, Y.; Vogt, B. D. Ultra-long cycle life, low-cost room temperature sodium-sulfur batteries enabled by highly doped (N,S) nanoporous carbons. *Nano Energy* **2017**, 32, 59–66.
- (19) Liu, Y.-T.; Zhu, X.-D.; Pan, L. Hybrid Architectures based on 2D MXenes and Low-Dimensional Inorganic Nanostructures: Methods, Synergies, and Energy-Related Applications. *Small* **2018**, *14*, No. 1803632
- (20) Wang, Y.; Lai, Y.; Chu, J.; Yan, Z.; Wang, Y.-X.; Chou, S.-L.; Liu, H.-K.; Dou, S. X.; Ai, X.; Yang, H.; Cao, Y. Tunable Electrocatalytic Behavior of Sodiated MoS₂ Active Sites toward Efficient Sulfur Redox Reactions in Room-Temperature Na—S Batteries. *Adv. Mater.* **2021**, 33, No. 2100229.
- (21) Hussain, T.; Kaewmaraya, T.; Hu, Z.; Zhao, X. S. Efficient Control of the Shuttle Effect in Sodium—Sulfur Batteries with Functionalized Nanoporous Graphenes. *ACS Appl. Nano Mater.* **2022**, *5*, 12637—12645.
- (22) Liu, H.; Sun, S.; Jin, B. Recent progress in MXenes-based lithium-sulfur batteries. *Energy Mater.* **2024**, *4*, 400053.
- (23) Li, N.; Zhan, Y.; Wu, H.; Fan, J.; Jia, J. Synergistically boosting the anchoring effect and catalytic activity of MXenes as bifunctional electrocatalysts for sodium—sulfur batteries by single-atom catalyst engineering. *Nanoscale* **2023**, *15*, 2747–2755.
- (24) Dai, X.-W.; Wang, Z.-R.; Wang, X.-L.; Chun, J.-Y.; Wei, C.-L.; Tan, L.-W.; Feng, J.-K. MXene-based sodium—sulfur batteries: synthesis, applications and perspectives. *Rare Met.* **2025**, *44*, 1522—1555.
- (25) Li, P.; Zhao, X.; Ding, Y.; Chen, L.; Wang, X.; Xie, H. Application studies on MXene-based flexible composites. *Front. Therm. Eng.* **2024**, 4, No. 1440165.
- (26) Zhou, Y.; Yin, L.; Xiang, S.; Yu, S.; Johnson, H. M.; Wang, S.; Yin, J.; Zhao, J.; Luo, Y.; Chu, P. K. Unleashing the Potential of MXene-Based Flexible Materials for High-Performance Energy Storage Devices. *Adv. Sci.* **2024**, *11*, No. 2304874.
- (27) An, Y.; Tian, Y.; Shen, H.; Man, Q.; Xiong, S.; Feng, J. Two-dimensional MXenes for flexible energy storage devices. *Energy Environ. Sci.* **2023**, *16*, 4191–4250.
- (28) Kumar, S.; Kumari, N.; Singh, T.; Seo, Y. Shielding 2D MXenes against oxidative degradation: recent advances, factors and preventive measures. *J. Mater. Chem. C* **2024**, *12*, 8243–8281.
- (29) Bhat, A.; Anwer, S.; Bhat, K. S.; Mohideen, M. I. H.; Liao, K.; Qurashi, A. Prospects challenges and stability of 2D MXenes for clean energy conversion and storage applications. *npj* 2D Mater. Appl. **2021**, *5*, 61.
- (30) Nahirniak, S.; Ray, A.; Saruhan, B. Challenges and Future Prospects of the MXene-Based Materials for Energy Storage Applications. *Batteries* **2023**, *9*, 126.
- (31) Liu, L.; Huang, L.; Yan, S.; Shi, W.; Li, S.; Chen, X.; Liu, J. Heteroatom doped S, N-MXene/rGO flexible film for supercapacitor applications. *Chem. Eng. J.* **2025**, *506*, No. 160320.
- (32) Rao, K. S.; Pathak, D. D.; Mandal, B. P.; Tyagi, A. K. MXene/rGO/sulfur loaded separator based current collector-free lithium sulfur batteries with high sulfur loading and cycle life. *J. Mater. Sci.: Mater. Electron.* **2024**, *35*, 1060.
- (33) Li, Y.-M.; Guo, Y.-L.; Jiao, Z.-Y. The effect of S-functionalized and vacancies on V_2C MXenes as anode materials for Na-ion and Li-ion batteries. *Curr. Appl. Phys.* **2020**, 20, 310–319.
- (34) Chen, Z.; Huang, S.; Yuan, X.; Gan, X.; Zhou, N. A comparative study of M₂CS₂ and M₂CO₂ MXenes as anode materials for lithium ion batteries. *Appl. Surf. Sci.* **2021**, *544*, No. 148861.
- (35) Siriwardane, E. M. D.; Demiroglu, I.; Sevik, C.; Peeters, F. M.; Çakır, D. Assessment of Sulfur-Functionalized MXenes for Li-Ion Battery Applications. *J. Phys. Chem. C* **2020**, *124*, 21293–21304.

- (36) Zhao, M.-Q.; Xie, X.; Ren, C. E.; Makaryan, T.; Anasori, B.; Wang, G.; Gogotsi, Y. Hollow MXene Spheres and 3D Macroporous MXene Frameworks for Na-Ion Storage. *Adv. Mater.* **2017**, *29*, No. 1702410.
- (37) Kresse, G.; Furthmüller, J. Efficient iterative schemes for ab initio total-energy calculations using a plane-wave basis set. *Phys. Rev. B* **1996**, 54, 11169–11186.
- (38) Perdew, J. P.; Burke, K.; Ernzerhof, M. Generalized Gradient Approximation Made Simple. *Phys. Rev. Lett.* **1996**, *77*, 3865–3868.
- (39) Grimme, S.; Antony, J.; Ehrlich, S.; Krieg, H. A consistent and accurate ab initio parametrization of density functional dispersion correction (DFT-D) for the 94 elements H-Pu. *J. Chem. Phys.* **2010**, 132, 154104.
- (40) Kresse, G.; Joubert, D. From ultrasoft pseudopotentials to the projector augmented-wave method. *Phys. Rev. B* **1999**, *59*, 1758–1775.
- (41) Monkhorst, H. J.; Pack, J. D. Special points for Brillouin-zone integrations. *Phys. Rev. B* **1976**, *13*, 5188–5192.
- (42) Wong, A. J. Y.; Lieu, W. Y.; Yang, H. Y.; Seh, Z. W. MXenes in sulfur cathodes for lithium—sulfur batteries. *J. Mater. Res.* **2022**, *37*, 3890—3905.
- (43) Henkelman, G.; Uberuaga, B. P.; Jónsson, H. A climbing image nudged elastic band method for finding saddle points and minimum energy paths. *J. Chem. Phys.* **2000**, *113*, 9901–9904.
- (44) Henkelman, G.; Arnaldsson, A.; Jónsson, H. A fast and robust algorithm for Bader decomposition of charge density. *Comput. Mater. Sci.* **2006**, *36*, 354–360.
- (45) Nelson, R.; Ertural, C.; George, J.; Deringer, V. L.; Hautier, G.; Dronskowski, R. LOBSTER: Local orbital projections, atomic charges, and chemical-bonding analysis from projector-augmented-wave-based density-functional theory. *J. Comput. Chem.* **2020**, *41*, 1931–1940.
- (46) Wang, V.; Xu, N.; Liu, J.-C.; Tang, G.; Geng, W.-T. VASPKIT: A user-friendly interface facilitating high-throughput computing and analysis using VASP code. *Comput. Phys. Commun.* **2021**, 267, No. 108033.
- (47) Wang, V.; Tang, G.; Liu, Y.-C.; Wang, R.-T.; Mizuseki, H.; Kawazoe, Y.; Nara, J.; Geng, W. T. High-Throughput Computational Screening of Two-Dimensional Semiconductors. *J. Phys. Chem. Lett.* **2022**, *13*, 11581–11594.
- (48) Jayan, R.; Islam, M. M. Mechanistic Insights into Interactions of Polysulfides at V₂ Interfaces in Na-S Batteries: A DFT Study. ACS Appl. Mater. Interfaces 2021, 13, 35848-35855.
- (49) Nahian, M. S.; Jayan, R.; Islam, M. M. Atomic-Scale Insights into Comparative Mechanisms and Kinetics of Na—S and Li—S Batteries. *ACS Catal.* **2022**, *12*, 7664—7676.
- (50) Assary, R. S.; Curtiss, L. A.; Moore, J. S. Toward a Molecular Understanding of Energetics in Li–S Batteries Using Nonaqueous Electrolytes: A High-Level Quantum Chemical Study. *J. Phys. Chem. C* **2014**, *118*, 11545–11558.
- (51) Jayan, R.; Islam, M. M. Design Principles of Bifunctional Electrocatalysts for Engineered Interfaces in Na-S Batteries. *ACS Catal.* **2021**, *11*, 15149–15161.
- (52) Yang, X.; Gao, X.; Sun, Q.; Jand, S. P.; Yu, Y.; Zhao, Y.; Li, X.; Adair, K.; Kuo, L.-Y.; Rohrer, J.; Liang, J.; Lin, X.; Banis, M. N.; Hu, Y.; Zhang, H.; Li, X.; Li, R.; Zhang, H.; Kaghazchi, P.; Sham, T.-K.; Sun, X. Promoting the Transformation of Li₂S₂ to Li₂S: Significantly Increasing Utilization of Active Materials for High-Sulfur-Loading Li—S Batteries. *Adv. Mater.* **2019**, *31*, No. 1901220.
- (53) Kaewmaraya, T.; Thatsami, N.; Tangpakonsab, P.; Klinkla, R.; Kotmool, K.; Hussian, T. Revealing the binding mechanism of redox intermediates in sodium—sulfur batteries by two-dimensional Janus monolayers. *J. Power Sources* **2023**, *585*, No. 233639.
- (54) Zhou, G.; Tian, H.; Jin, Y.; Tao, X.; Liu, B.; Zhang, R.; Seh, Z. W.; Zhuo, D.; Liu, Y.; Sun, J.; Zhao, J.; Zu, C.; Wu, D. S.; Zhang, Q.; Cui, Y. Catalytic oxidation of Li₂S on the surface of metal sulfides for Li–S batteries. *Proc. Natl. Acad. Sci. U. S. A.* **2017**, *114*, 840–845.
- (55) Dronskowski, R.; Bloechl, P. E. Crystal orbital Hamilton populations (COHP): energy-resolved visualization of chemical bonding in solids based on density-functional calculations. *J. Phys. Chem.* **1993**, *97*, 8617–8624.

- (56) Naik, A. A.; Ertural, C.; Dhamrait, N.; Benner, P.; George, J. A Quantum-Chemical Bonding Database for Solid-State Materials. *Sci. Data* **2023**, *10*, 610.
- (57) Yao, Z.; Zou, Y.; Liu, S.; Li, Y.; Guo, Q.; Zheng, C.; Sun, W. Reactivity descriptors for sulfur redox kinetics in lithium—sulfur batteries: from mechanistic insights to machine learning driven catalyst design. *Chem. Soc. Rev.* **2025**, *54*, 9161–9191.
- (58) Yu, X.; Yang, Y.; Si, L.; Cai, J.; Lu, X.; Sun, Z. $V_4C_3T_x$ MXene: First-principles computational and separator modification study on immobilization and catalytic conversion of polysulfide in Li-S batteries. *J. Colloid Interface Sci.* **2022**, 627, 992–1002.
- (59) Mouhat, F.; Coudert, F.-X. Necessary and sufficient elastic stability conditions in various crystal systems. *Phys. Rev. B* **2014**, *90*, No. 224104.
- (60) Liu, L.; Zhang, J.; Zhao, J.; Liu, F. Mechanical properties of graphene oxides. *Nanoscale* **2012**, *4*, 5910–5916.
- (61) Lipatov, A.; Lu, H.; Alhabeb, M.; Anasori, B.; Gruverman, A.; Gogotsi, Y.; Sinitskii, A. Elastic properties of 2D Ti₃C₂T_x MXene monolayers and bilayers. *Sci. Adv.* **2018**, *4*, No. eaat0491.
- (62) Zhao, Y.; Li, B.; Tian, C.; Han, X.; Qiu, Y.; Xiong, H.; Li, K.; Hou, C.; Li, Y.; Wang, H.; Zhang, Q. Anhydrous organic etching derived fluorine-rich terminated MXene nanosheets for efficient and stable perovskite solar cells. *Chem. Eng. J.* 2023, 469, No. 143862.
- (63) Lam, D. V.; Nguyen, V. H.; Yoo, H.; Dung, D. T.; Syed, S. A.; Ha, J.; Oh, W.; Lee, S.-M.; Oh, I.-K. Dry Synthesis of Sulfur-Terminated MXene as Multifunctional Catalyst for Stable Lithium—Sulfur Batteries. *Small* **2025**, *21*, No. 2411668.
- (64) Zhou, Y.; Maleski, K.; Anasori, B.; Thostenson, J. O.; Pang, Y.; Feng, Y.; Zeng, K.; Parker, C. B.; Zauscher, S.; Gogotsi, Y.; Glass, J. T.; Cao, C. Ti₃C₂T_x MXene-Reduced Graphene Oxide Composite Electrodes for Stretchable Supercapacitors. *ACS Nano* **2020**, *14*, 3576–3586.
- (65) Hegde, S.; Hakkeem, H.; Alagar, S.; Baasanjav, E.; Rout, C. S.; Jeong, S. M. Laser-driven engineering of modulated structural defects in Nb₂CT_x MXene-rGO based flexible microsupercapacitors for energy storage application. *J. Energy Storage* **2025**, *111*, No. 115330.
- (66) Jena, S.; Laha, S.; Swain, B. P. Ti₂NT_x MXene/rGO nanocomposites: Optical tunning, functional bonding and electrochemical analysis for supercapacitor electrode application. *Appl. Surf. Sci.* **2024**, 666, No. 160403.
- (67) Wu, M.; Wang, B.; Hu, Q.; Wang, L.; Zhou, A. The Synthesis Process and Thermal Stability of V_2C MXene. *Materials* **2018**, 11, 2112. (68) Li, X.; Li, M.; Xu, W.; Huang, Z.; Liang, G.; Yang, Q.; Huang, Q.; Zhi, C. V_2CTx MXene Sphere for Aqueous Ion Storage. *Energy Mater. Adv.* **2023**, 4, No. 0066.
- (69) Zhang, H.; Shen, L.; Geng, X.; Zhang, J.; Jiang, Y.; Ma, H.; Liu, Q.; Yang, K.; Ma, J.; Zhu, N. MXene-rGO aerogel assisted Na_{3.5}MnTi(PO₄)₃ cathode for high-performance sodium-ion batteries. *Chem. Eng. J.* **2023**, *466*, No. 143132.
- (70) Zahra, S. A.; Murshed, M. M.; Naeem, U.; Gesing, T. M.; Rizwan, S. Cation-assisted self-assembled pillared V_2CT_x MXene electrodes for efficient energy storage. *Chem. Eng. J.* **2023**, 474, No. 145526.



CAS BIOFINDER DISCOVERY PLATFORM™

STOP DIGGING THROUGH DATA —START MAKING DISCOVERIES

CAS BioFinder helps you find the right biological insights in seconds

Start your search

